

Article

Self-Supported Co_3O_4 @Mo- Co_3O_4 Needle-like Nanosheet Heterostructured Architectures of Battery-Type Electrodes for High-Performance Asymmetric Supercapacitors

Yedluri Anil Kumar ^{1,2,†} , Himadri Tanaya Das ³ , Phaneendra Reddy Guddeti ⁴ ,
Ramesh Reddy Nallapureddy ^{5,†}, Mohan Reddy Pallavolu ^{5,*} , Salem Alzahmi ^{2,6}  and Ihab M. Obaidat ^{1,2,*}

¹ Department of Physics, United Arab Emirates University, Al Ain 15551, United Arab Emirates; yedluri.anil@gmail.com

² National Water and Energy Center, United Arab Emirates University, Al Ain 15551, United Arab Emirates; s.alzahmi@uaeu.ac.ae

³ Centre of Advanced Materials and Applications, Utkal University, Vanivihar, Bhubaneswar 751004, India; himadridas@utkaluniversity.ac.in

⁴ Department of Physics, Sri Venkateswara Vedic University, Tirupati 517502, India; phaneendra369@gmail.com

⁵ School of Chemical Engineering, Yeungnam University, Gyeongsan 38541, Korea; rameshsun999@gmail.com

⁶ Department of Chemical & Petroleum Engineering, United Arab Emirates University, Al Ain 15551, United Arab Emirates

* Correspondence: pmreddy@yu.ac.kr (M.R.P.); iobaidat@uaeu.ac.ae (I.M.O.)

† These authors contributed equally to this work.



Citation: Kumar, Y.A.; Das, H.T.; Guddeti, P.R.; Nallapureddy, R.R.; Pallavolu, M.R.; Alzahmi, S.; Obaidat, I.M. Self-Supported Co_3O_4 @Mo- Co_3O_4 Needle-like Nanosheet Heterostructured Architectures of Battery-Type Electrodes for High-Performance Asymmetric Supercapacitors. *Nanomaterials* **2022**, *12*, 2330. <https://doi.org/10.3390/nano12142330>

Academic Editors: Jeng-Yu Lin, Min-Hsin Yeh and Tzu-Ho Wu

Received: 22 June 2022

Accepted: 4 July 2022

Published: 7 July 2022

Publisher's Note: MDPI stays neutral with regard to jurisdictional claims in published maps and institutional affiliations.



Copyright: © 2022 by the authors. Licensee MDPI, Basel, Switzerland. This article is an open access article distributed under the terms and conditions of the Creative Commons Attribution (CC BY) license (<https://creativecommons.org/licenses/by/4.0/>).

Abstract: Herein, this report uses Co_3O_4 nanoneedles to decorate Mo- Co_3O_4 nanosheets over Ni foam, which were fabricated by the hydrothermal route, in order to create a supercapacitor material which is compared with its counterparts. The surface morphology of the developed material was investigated through scanning electron microscopy and the structural properties were evaluated using XRD. The charging storage activities of the electrode materials were evaluated mainly by cyclic voltammetry and galvanostatic charge-discharge investigations. In comparison to binary metal oxides, the specific capacities for the composite Co_3O_4 @Mo- Co_3O_4 nanosheets and Co_3O_4 nano-needles were calculated to be 814, and 615 C g^{-1} at a current density of 1 A g^{-1} , respectively. The electrode of the composite Co_3O_4 @Mo- Co_3O_4 nanosheets displayed superior stability during 4000 cycles, with a capacity of around 90%. The asymmetric Co_3O_4 @Mo- Co_3O_4 //AC device achieved a maximum specific energy of 51.35 Wh Kg^{-1} and power density of 790 W kg^{-1} . The Co_3O_4 @Mo- Co_3O_4 //AC device capacity decreased by only 12.1% after 4000 long GCD cycles, which is considerably higher than that of similar electrodes. All these results reveal that the Co_3O_4 @Mo- Co_3O_4 nanocomposite is a very promising electrode material and a stabled supercapacitor.

Keywords: Co_3O_4 @Mo- Co_3O_4 nanocomposite; binder free electrode; supercapacitor; hydrothermal; energy storage

1. Introduction

With broad applicability in the electronics, power systems, communication systems, and automobile sectors, supercapacitors have been recognized as being highly reliable among the numerous forms of energy storage devices. Supercapacitors exhibit high power densities and high charge storage abilities with long-term stability compared to batteries [1]. The cost-effective and less hazardous properties of supercapacitor components have motivated researchers to explore different electrode materials. Still, the practical usability of supercapacitors is limited due to their low energy densities for which battery-type electrodes are currently preferred. A wide range of transition mono-/multi-metallic oxides or hydroxides has been investigated as electrode materials for supercapacitors [2,3]. Among these, cobalt oxides have been found to possess high theoretical specific capacities [4].

The electrochemical properties of cobalt oxides can be improved by different strategies like tuning their morphology, doping with other metals, creating oxygen vacancies, etc. The tuning morphology is governed by the synthesis process, temperature, concentration, and reaction time. Among the various synthesis processes, the hydrothermal method is an old technique for synthesizing various nanomaterials. Interestingly, nanomaterials derived from hydrothermal methods with different shapes and sizes, dopants, core-shell, heterostructures, etc. have been found to be efficient for energy storage applications [5,6].

It has been reported that CoMoO_4 hexagonal 2D-nanosheets have high charge storage capabilities [7]. Such bimetallic oxides also have the advantage of the synergetic effect of both metals, where either both metals take part in redox reactions or one of them supports the electrochemical reaction of the other. Interestingly, oxygen vacancies are created in CoMoO_{4-x} by hydrogenation of the hydrothermally obtained CoMoO_4 [8]. A theoretical study discovered that the oxygen vacancies have improved carrier density, thus increasing the electronic conductivity. The oxygen vacancy also acts as an active site for OH^- intake and accelerates the charge transfer kinetics. Another strategy, i.e., doping the parent nanomaterial, has been widely explored due to the cost-effective approach to synthesis and ease of tuning the properties which it offers. For example, rare-earth metal (La, Nd, Gd, Sm) doping of Co_3O_4 synthesized by the polymer combustion method was employed for the study of the transfer of ions and electrons in supercapacitors [9]. Mo-doping of Co_3O_4 by various methods (sol-gel, electrodeposition, and hydrothermal) has been investigated as a means to synthesize potential electrode materials [10,11]. Shen et al. developed Mo- Co_3O_4 nanosheets as a battery-type electrode for supercapacitor applications and reported a specific capacity of 128.2 mAh/g at 1 A/g with 95% of capacity retention after long-term cyclings [12]. The experimental results were substantiated by theoretical calculations; it was shown that Mo-doping of Co_3O_4 modifies the bandgap and increases the electronic conductivity of the parent material, which enhances charge storage capability.

Recently, heterostructures have been designed as electrode materials for supercapacitors due to their extraordinary electrochemical performance and self-supported nanostructures with high structural and chemical stability [13]. A core-shell of hierarchical 3D $\text{NiCo}_2\text{O}_4@ZnWO_4$ was synthesized by the hydrothermal method for an all-solid-state symmetric supercapacitor (SSC) [14]. A multicomponent $\text{MnMoO}_4/\text{MnCO}_3$ hybrid synthesized by a one-step hydrothermal method with urea as the reaction fuel was found to store ample charge with good reversibility [15]. Zhao et al. engineered Fe_2O_3 nanoneedle arrays with typical mesoporous structures and $\text{NiCo}_2\text{O}_4/\text{Ni}(\text{OH})_2$ hybrid nanosheet arrays on SiC nanowire skeletons for asymmetric supercapacitors [16]. Binary heterojunction nanocomposites of $\text{CoTiO}_3@Co_3O_4/\text{N}$ -single bond CNO matrix were established with excellent electrochemical properties [17]. Similarly, a hybrid, interconnected structure of nanoplates and nanowires of NiCo_2O_4 was found to have large surface area to support redox reactions [18]. A nanocomposite of needle-like Co_3O_4 and graphitic N-CNOs nanosheets was synthesized by a simple solvothermal and pyrolysis method [19]; it showed very high specific capacitance and good rate capability. Further, the asymmetric device with activated carbon (AC) showed good energy density and Coulombic efficiency. Such work proves that needle-like nanostructures along with nanosheets are appropriate electrodes for supercapacitors. There are many advantages of using nanomaterials, such as: (i) large surface area; (ii) synergistic charge storage; (iii) more electroactive sites exposed to the electrolyte; and (iv) time and cost-saving production.

In this work, a $\text{Co}_3\text{O}_4@Mo\text{-Co}_3\text{O}_4$ nanosheet composite heterostructure was synthesized by hydrothermal and pyrolysis method. As a result of the synergistic redox features between the Co_3O_4 nano-needles and $Mo\text{-Co}_3\text{O}_4$ nanosheets, the $\text{Co}_3\text{O}_4@Mo\text{-Co}_3\text{O}_4$ electrode displayed superior electrochemical activities with a specific capacity of 814 C g^{-1} (1 A g^{-1}) and retention of 90% after 4000 long-cycles. In addition, an asymmetric supercapacitor (ASC) with continuous cycling stability was assembled utilizing $\text{Co}_3\text{O}_4@Mo\text{-Co}_3\text{O}_4$ and activated carbon (AC). The fabricated $\text{Co}_3\text{O}_4@Mo\text{-Co}_3\text{O}_4//AC$ ASC displayed great electrochemical capacity, stability, and superior conductivity.

2. Experiment Procedure

2.1. Chemical Details

All chemicals were purchased from Sigma Aldrich and used without further processing. Cobalt nitrate hexahydrate ($\text{Co}(\text{NO}_3)_2 \cdot 6\text{H}_2\text{O}$), sodium molybdate (NaMoO_4), and urea were used to synthesize the electrode material. N-Methyl-2-pyrrolidone (NMP, analytical grade), polyvinylidene fluoride (PVDF, analytical grade), nickel (Ni) foam, and activated carbon (AC, analytical grade) were used for electrode fabrication.

2.2. Synthesis of Co_3O_4 and $\text{Co}_3\text{O}_4@Mo\text{-Co}_3\text{O}_4$

The hetero-structure nanomaterial was synthesized via a facile hydrothermal method followed by low-temperature calcination. Pure precursors, i.e., cobalt nitrate, sodium molybdate, and urea, were used as-purchased. First, 2 mmol of $\text{Co}(\text{NO}_3)_2 \cdot 6\text{H}_2\text{O}$ (0.582 g), 1 mMol NaMoO_4 (0.206 g), and 10 mM urea (0.6 g) were completely dissolved in distilled water (25 mL) and ethanol (10 mL). Then, the 35-mL solution was transferred to a Teflon-lined autoclave for hydrothermal synthesis. The autoclave was subjected to heating to 120 °C and maintained for 10 h. Then, the autoclave was cooled to room temperature. The hydrothermal sample was washed with distilled water and ethanol to remove unreacted precursors or impurities, followed by drying at 60 °C. Finally, the obtained powder was calcinated at 350 °C for 3 h at a heating rate of 5 °C/min. Figure 1 presents a schematic view of the synthesis of the heterostructured Co_3O_4 nanoneedles and $\text{Mo-Co}_3\text{O}_4$ nano-petals. The low temperature used in the hydrothermal treatment allowed nucleation and the growth of nanoneedles and nanosheets to occur, while the post-annealing improved the crystallinity of the synthesized oxides.

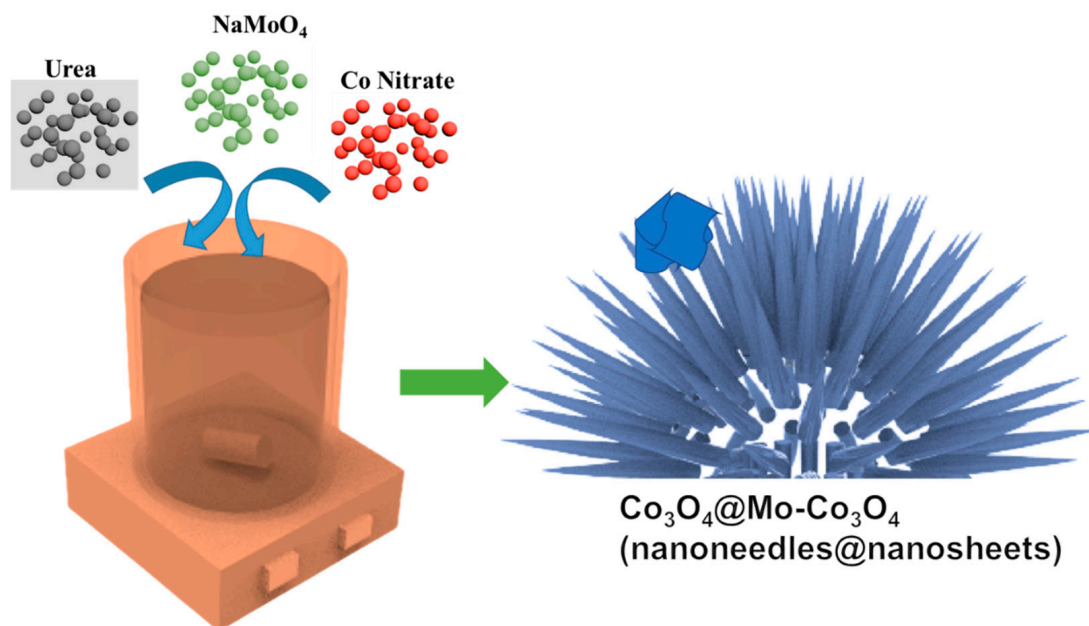


Figure 1. Schematic of $\text{Co}_3\text{O}_4@Mo\text{-Co}_3\text{O}_4$ needle-like nanosheets, synthesized by hydrothermal method.

2.3. Characterizations

Detailed characterizations and an electrochemical analysis are available in the supporting file. In addition, the device fabrication procedure and calculation method of the specific capacity, energy, and power densities are provided and applied to the methods and calculations reported in previous literature [15,17,19–21].

2.4. Asymmetric Supercapacitor Preparation

For a three-electrode configuration, Co_3O_4 and $\text{Mo-Co}_3\text{O}_4$ coated on Ni foam were utilized as a working electrode, platinum wire as a counter electrode, and Ag/AgCl as a

reference electrode, with 2.0 M KOH as the active electrolyte. For a two-electrode setup, Mo-Co₃O₄ coated on Ni foam was utilized as a positive electrode and activated carbon (AC) as a negative electrode, while Whatman filter paper—dipped in 2 M KOH solution and then placed between the positive and negative electrodes—was used as a separator. The mass-loading in the three-electrode setup was around 3 mg; in the two-electrode setup, an active mass of 8.7 mg was loaded onto the positive electrode (M) and 1 mg was loaded onto the negative electrode (AC). These values were chosen to balance the charge on both electrodes. The CV measurements for the ASC device were carried out in the potential range of −0.1 to 0.6 V at various scanning rates from 10 to 30 mV s^{−1}, whereas GCD characterizations were performed in potential ranges from 0 to 1.6 V at various current densities, i.e., ranging from 1 to 10 A g^{−1}. Moreover, EIS studies for both the two and three-electrode setups were carried out with an open circuit potential (OCP) ranging from 1 Hz to 100 kHz, with an AC perturbation of 5 mV.

In a three-electrode setup, the specific capacities were calculated from the GCD curves using the below equation:

$$C = \frac{I \cdot \Delta t}{m} \quad (1)$$

where C is the specific capacity (C/g), I indicates the discharge current (A), Δt is the discharge time (s), and m represents the mass of the active material (g). In the two-electrode setup, the specific capacitance (measured from GCD plots) of the active electrodes was calculated from the following equation:

$$C_s = \frac{I \cdot \Delta t}{m \cdot \Delta V} \quad (2)$$

To assemble the supercapacitor device, the charge stored on the positive and negative electrodes was described by $q^+ = q^-$. The mass balance of the positive and negative electrodes was estimated by:

$$\frac{m_+}{m_-} = \frac{C_s \cdot x \Delta V_-}{C_s \cdot x \Delta V_+} \quad (3)$$

Also, in the two-electrode setup, the energy density (Wh/Kg) and power density (W/Kg) were measured as follows:

$$E = \frac{1}{2} C_s (\Delta V)^2 \quad (4)$$

$$P = \frac{E}{\Delta t} \quad (5)$$

where C_s is the specific capacitances (F/g), Δt is the discharge time (s), ΔV is the operating voltage window (V), m is the active mass of the working material (g), E is the energy density (Wh/kg), and P is the power density (W/kg).

3. Results and Discussion

The X-ray diffraction patterns of Co₃O₄ and Mo-Co₃O₄ were studied in the 2 θ range of 10–80°, as presented in Figure 2a. The diffraction patterns demonstrated that the prepared heterostructure was polycrystalline, presenting several peaks which were consistent with Co₃O₄ planes. The diffraction patterns of the Co₃O₄ and Mo-Co₃O₄ heterostructure showed peaks at the (220), (311), (400), (511), and (440) planes, which corresponded to the cubic crystal structure of the Co₃O₄ phase. All of the planes matched with the JCPDS card no: 042-1467 [19]. The diffraction pattern showed no peaks corresponding to cobalt or molybdenum, indicating that no extra phases existed in the heterostructure. The XRD pattern of the Mo-doped Co₃O₄ heterostructure exhibited an additional peak at the (002) plane. Irrespective of the (002) plane, all the remaining planes showed pure Co₃O₄, indicating that no structural deformation had occurred in the host Co₃O₄ lattice upon Mo-doping.

This demonstrates that Mo ions were successfully substituted in the Co lattice positions in the Co_3O_4 matrix.

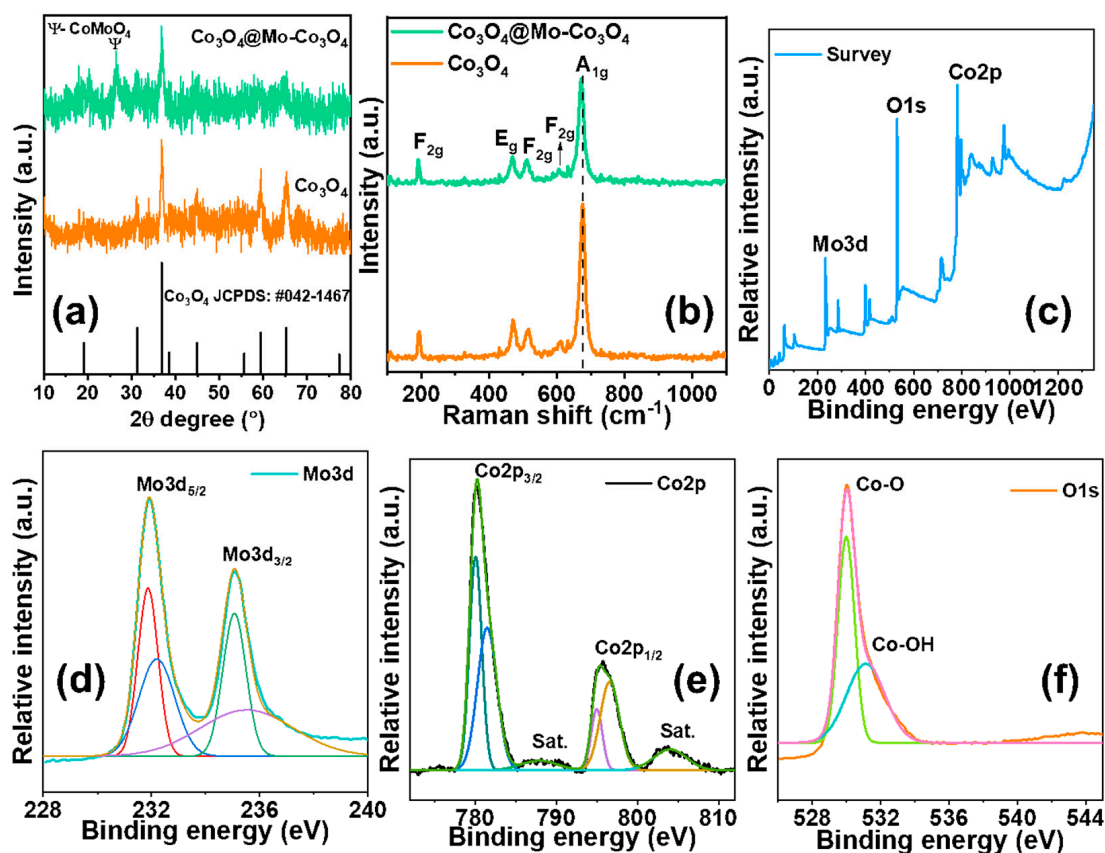


Figure 2. (a,b) XRD pattern and Raman spectra of Co_3O_4 and $\text{Co}_3\text{O}_4@Mo\text{-Co}_3\text{O}_4$ needle-like nanosheet heterostructure, (c) XPS survey spectra of $\text{Co}_3\text{O}_4@Mo\text{-Co}_3\text{O}_4$, (d) deconvoluted high-resolution spectra of Mo3d, (e) deconvoluted high-resolution spectra of Co2p, and (f) deconvoluted high-resolution spectra of O1s.

Rietveld refinement was also used to determine the presence of Mo in the Co_3O_4 lattice for the $\text{Co}_3\text{O}_4@Mo\text{-Co}_3\text{O}_4$ heterostructure. In this analysis, R weighted profile (R_{wp}), R profile (R_p), R structure factor, R Bragg factor (R_{Bragg}), and goodness of fit (GOF) structural parameters were evaluated (as shown in Figure S1) using the EXPO software. The unit cell parameters were also calculated using the Rietveld refinement results. Table 1 shows the estimated Rietveld refinement parameters, including R_p , R_{wp} , GOF, R structure factor, R_{Bragg} , and the unit cell parameters. The quality of Mo substitution in the Co_3O_4 matrix can be determined from the GOF value, which is 0.805.

Table 1. Estimated lattice structure parameters and refinement parameter values from Rietveld refinement of $\text{Co}_3\text{O}_4@Mo\text{-Co}_3\text{O}_4$ heterostructure.

Unit Cell Parameters	
a , (Å)	8.08
b , (Å)	8.08
c , (Å)	8.08
α , (°)	90
β , (°)	90
γ , (°)	90
Cell volume (Å ³)	528.24
Density (g/cm ³)	6.05

Table 1. Cont.

Unit Cell Parameters	
Crystal system and Space group number	Cubic & (Fd-3m, 227)
Structure parameters	
Atoms	130
Bonds	168
Polyhedra	34
Refinement parameters	
R _p	1.762
R _{wp}	2.216
Goodness of fit (GOF)	0.805
R-Structure factor	4.68
R-Bragg factor	6.89

Table 2 displays the site occupancy values of ions distributed with the corresponding fractional coordinate values. Co₃O₄ contains three Co sites (Co1, Co2, Co3) and two O sites (O1 and O2). The unit cell lattice parameters are included in Table 1. Further, the crystal structure and atomic bonding in Co₃O₄ were evaluated using the Vesta software. Co₃O₄ demonstrated a cubic crystal structure with space group Fd-3m (space group number: 227), with 130 atoms distributed with 168 bonds. Table 2 lists the structural parameters, while Figure 2 depicts the crystal structure.

Table 2. Site occupancies of various ions along with their fractional coordinates.

Element	X	Y	Z	Occupancy	Site	Sym.
O1	0.14000	0.14000	0.14000	1.000	16e	0.3 m
O2	0.61000	0.61000	0.61000	1.000	16e	0.3 m
Co1	0.75000	0.75000	0.75000	1.000	4d	−43 m
Co2	0.00000	0.00000	0.00000	1.000	4a	−43 m
Co3	0.37500	0.37500	0.37500	1.000	16e	0.3 m

Figure 2b shows Raman spectra of the Co₃O₄ and Co₃O₄@Mo-Co₃O₄ heterostructure. The Raman spectrum of intense peaks showed the Mo-O-Co stretching vibrations for Co₃O₄@Mo-Co₃O₄. The intense peaks in both samples may have arisen due to the vibrations of Co-O bonds representing the breathing mode of point phonons in the A_{1g} symmetry [5]. Several small peaks appeared due to the scattering of the F_{2g} or E_g phonons [7]. These bands can be integrated into Mo-O-Mo, Mo-O, and MoO₄ vibrations [8]. The results suggest that the synthesis of the Co₃O₄@Mo-Co₃O₄ heterostructure composite was successful.

In addition, FTIR analysis was performed on the Co₃O₄@Mo-Co₃O₄ needle-like nanosheet heterostructure for additional phase evolution, as presented in Figure S2. This is the first reported FTIR analysis of Mo-doped Co₃O₄ in a supercapacitor-related publication. The sharp peaks at 560 and 665 cm^{−1} correspond to pure Co₃O₄, comprising Co-O stretching vibrations [22]. These two bands confirm the presence of Co₃O₄, which is related to the OB3 vibration (B = Co³⁺ in an octahedral hole); the other band is related to the ABO₃ vibration (A = Co²⁺ in a tetrahedra hole) [23]. The small peaks at around 3425 and 1645 cm^{−1} resulted from the O-H groups [24]. The shift could be observed for the Mo-doped Co₃O₄, and was attributed to a change in the surface area as well as a surface defect due to the doping [25]. The peak at 1058 cm^{−1} belonged to the carbonate groups which resulted from air contamination during the reaction of oxide with CO₂ [26].

The chemical composition and valence state of the Co₃O₄@Mo-Co₃O₄ needle-like nanosheet heterostructure were analyzed using X-ray photoelectron spectroscopy (XPS), revealing the oxidation state of the transition metal ion. Figure 2c displays the spectra of Mo-Co₃O₄, showing Mo, Co, and O peaks in addition to C. The core-level photoelectron spectra of Mo3d, Co2p, and O1s are presented in Figure 2d–f. The Mo3d core transition

was considered by a doublet due to the spin-orbit coupling resulting from the $3d_{5/2}$ and $3d_{3/2}$ components. The binding energies of $Mo3d_{5/2}$ and $Mo3d_{3/2}$ were 231.92 ± 0.1 eV and 235.06 ± 0.1 eV, respectively. The local structure of the Mo atoms in the Co_3O_4 lattice offered information about its chemical state and was primarily responsible for these peak placements. The detected binding energy values of Mo differed from those of Mo-O-related compounds, indicating that the Mo cations had been perfectly substituted in the Co sites of the cubic structure.

Figure 2c shows two distinct peaks at 780.15 ± 0.1 eV and 795.64 ± 0.1 eV, which belong to $2p_{3/2}$ and $2p_{1/2}$, respectively. The energy difference between the Co $2p_{3/2}$ and $2p_{1/2}$ splitting was 15.49 eV, which indicated the existence of Co^{2+} and corresponded to the existence of Co_3O_4 . It can be noted that the binding energy difference ΔE between the $Co2p_{1/2}$ and $Co2p_{3/2}$ (15 eV) observed in the complex was equal to that found for Co(III), which was in agreement with the reported value [27]. The peak detected at 530.26 ± 0.1 eV was attributable to O1s linked to Co and Mo atoms in the lattice oxygen (see Figure 2d). Because the activation energy for oxygen diffusion is substantially higher than that for interstitial Co atoms and Mo^{6+} ions, enough oxygen atoms from the atmosphere can diffuse into the Co_3O_4 lattice to fill up the new oxygen vacancies created by the increase of Co(III) and Mo^{6+} ions during $Mo:Co_3O_4$ development. The existence of Co and O in XPS spectra is consistent with the XRD patterns.

The morphology of $Co_3O_4@Mo-Co_3O_4$ was characterized by FESEM, as shown in Figure 3. The one-pot hydrothermal synthesized $Co_3O_4@Mo-Co_3O_4$ was found to be heterostructured. It is worth mentioning that the heterostructures composed of the monolayer Co_3O_4 and some $Mo-Co_3O_4$ nanosheets demonstrated eminent structural formation. The images in Figure 3a–f show the $Co_3O_4@Mo-Co_3O_4$ at different magnifications. A bundle of nanoneedles of Co_3O_4 was arranged over a bud to give a flower-like nanostructure, while the $Mo-Co_3O_4$ nanosheets were stuck on/in the nanoneedles. The fact that the self-supported heterostructure formed without the addition of any surfactant or template is quite interesting. The Co_3O_4 and $Mo-Co_3O_4$ heterostructures exhibited excellent metallic characteristics and great structural stability, delivering better electronic conductivity and structural integrity than pristine composites. Moreover, self-assembled particles reduce the surface energy, enhancing the stability of the structure. Within the hierarchical heterostructures, both core and shell are active materials, and the core-shell heterostructures enable easy access to electrolytes. Therefore, both of them can effectively contribute to the capacity. Figure 3g shows the EDS spectra obtained for the elemental studies, whereas Figure 3h–j shows the elemental mapping for the Mo, Co, and O present in the $Co_3O_4@Mo-Co_3O_4$ needle-like nanosheet heterostructure. It is expected that the architecture can be beneficial for boosting electrochemical performance.

HRTEM images of the $Co_3O_4@Mo-Co_3O_4$ heterostructure are depicted in Figure 4, where the resolutions in a, b, and c are 50, 10, and 5 nm, respectively. Figure 4a,b clearly convey that there are different shapes of nanoneedles, i.e., a flower and small sheets attached to it. It was observed that the wide exposed nanoneedles in flower form provided space for the small sheets inside them, as well as sharp tips to hold nanosheets. Thus, the hydrothermal growth of the heterostructured Co_3O_4 nanoneedles and $Mo-Co_3O_4$ nanoplates resulted in the creation of interesting nanostructured electrode materials. The highest resolution image (Figure 4c) shows fringes, where the SAED pattern (inset in Figure 4c) confirms the highly crystalline nature of the hetero-structured nanomaterials. The precise spacings of 0.24, 0.29, and 0.46 nm were well-matched with the (311), (220), and (111) planes of $Mo-Co_3O_4$. The well-organized rings and dots seen in the SAED pattern prove the crystallinity nature of the electrode materials that could be beneficial in structure retention for long-term stability. There is no doubt that such an architecture would support efficient electrochemical performance in supercapacitor applications.

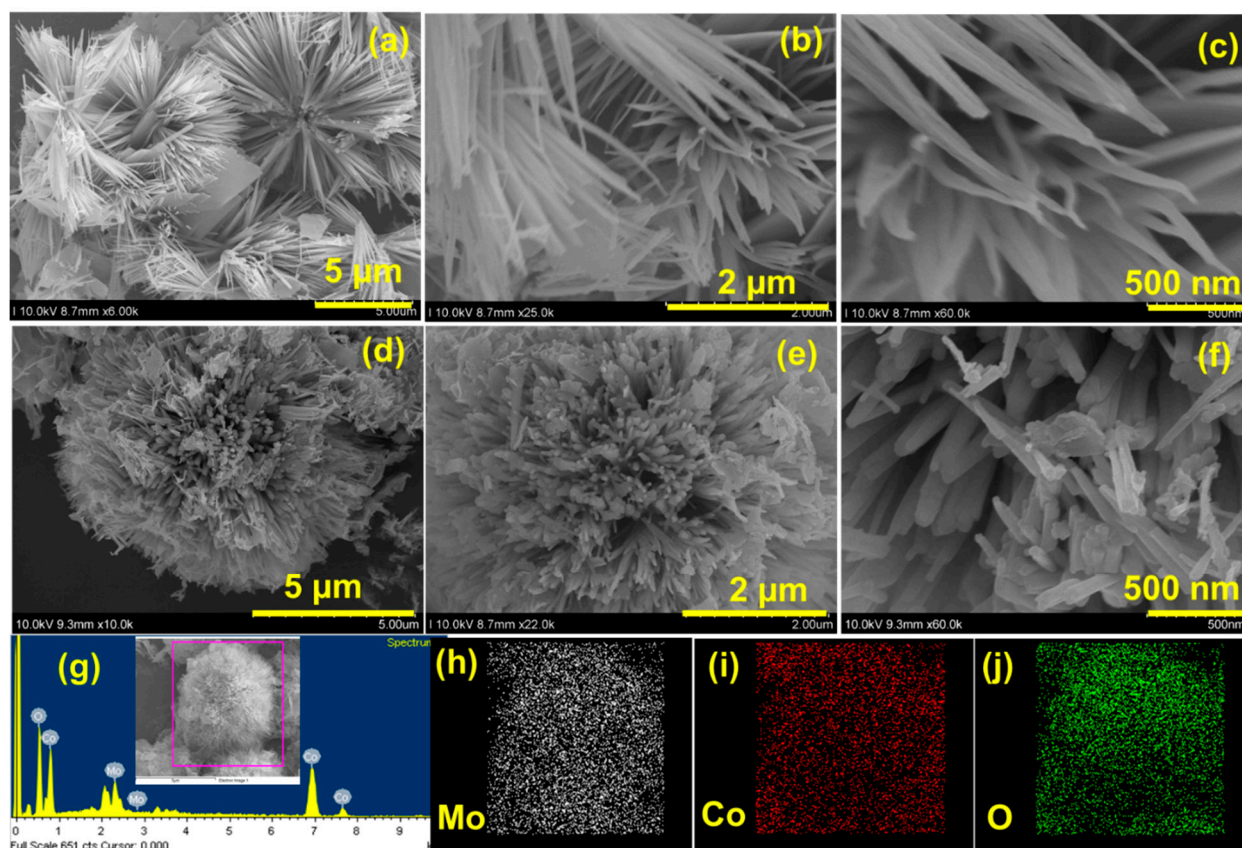


Figure 3. (a–f) FE-SEM images of $\text{Co}_3\text{O}_4@Mo\text{-Co}_3\text{O}_4$ needle-like nanosheet heterostructure at different magnifications, (g) EDS spectra: inset mapping image of $\text{Co}_3\text{O}_4@Mo\text{-Co}_3\text{O}_4$, (h) elemental map of Mo, (i) elemental map of Co, and (j) elemental map of O.

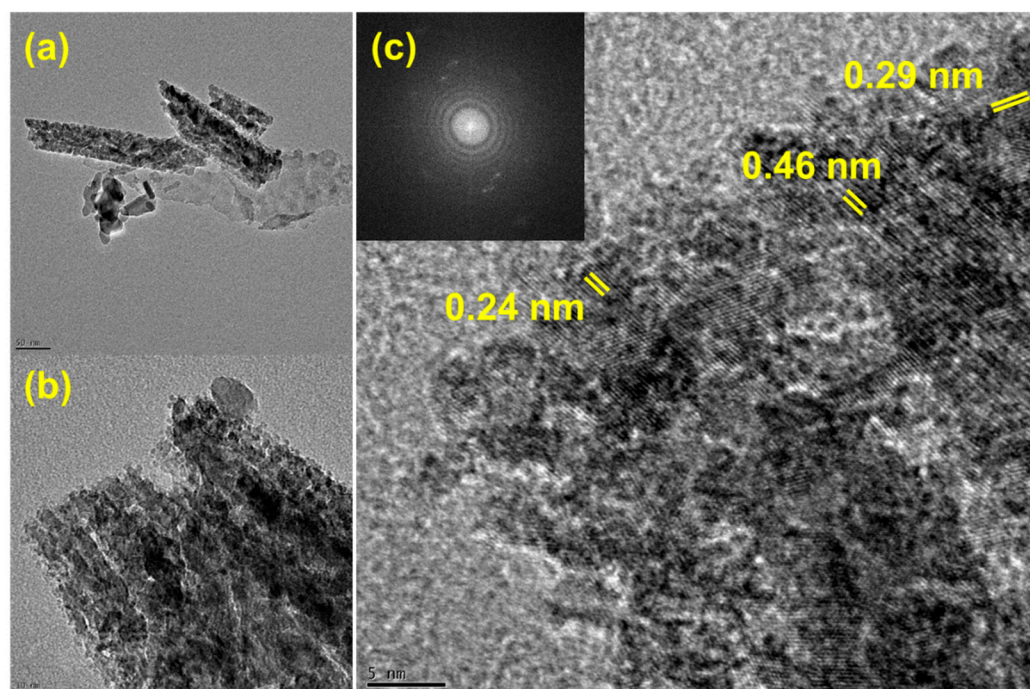


Figure 4. (a,b) TEM images at different magnifications, (c) high-resolution TEM image of $\text{Co}_3\text{O}_4@Mo\text{-Co}_3\text{O}_4$ needle-like nanosheet heterostructure: inset SAED pattern.

3.1. Electrochemical Properties of Electrode Materials

The hydrothermally obtained heterostructures were tested for three-electrode system electrochemical performance in 2M KOH electrolytes. Figure 5 illustrates a comparison of the Co_3O_4 and $\text{Co}_3\text{O}_4@\text{Mo-Co}_3\text{O}_4$ needle-like nanosheet heterostructure electrodes. It was found that the doping of Mo into Co_3O_4 enhanced the electrochemical properties, such as peak current and discharge time (Figure 5a,b). Notably, the cyclic voltammetry (CV) curves and the galvanic charge-discharge (GCD) curves demonstrated that doping did not shift the redox peaks of the Co_3O_4 . This indicated that Co_3O_4 undergoes redox reactions while Mo facilitates the electrochemical performance of Co_3O_4 . The CV curves in the potential window of -0.1 to 0.6 V at different scan rates, i.e., 10 – 30 mV/s, obtained for Co_3O_4 and the $\text{Co}_3\text{O}_4@\text{Mo-Co}_3\text{O}_4$ heterostructures, are shown in Figure 6c,d. At each scan rate, clear oxidation and reduction peaks (0.35 V and 0.2 V) were found in the same place, with an increase in the current density with increasing scan rate. Figure 5e,f presents the GCD profiles in a potential window of 0 to 0.45 V at different current densities, i.e., 1 – 10 A/g, obtained for Co_3O_4 and the $\text{Co}_3\text{O}_4@\text{Mo-Co}_3\text{O}_4$ heterostructure. The battery-type behavior is clearly visible in the plateau-like charge/discharge pattern. The Co_3O_4 and $\text{Co}_3\text{O}_4@\text{Mo-Co}_3\text{O}_4$ heterostructure revealed similar humps, indicating the occurrence of redox reactions due to cobalt, where Mo- Co_3O_4 has a higher discharge time than Co_3O_4 . The Mo atoms did not show redox activity during charge/discharge reactions but promoted electrochemical performance. The calculated specific capacity is given in Figure 5g. The faradaic reactions for Co_3O_4 are given below [28]:

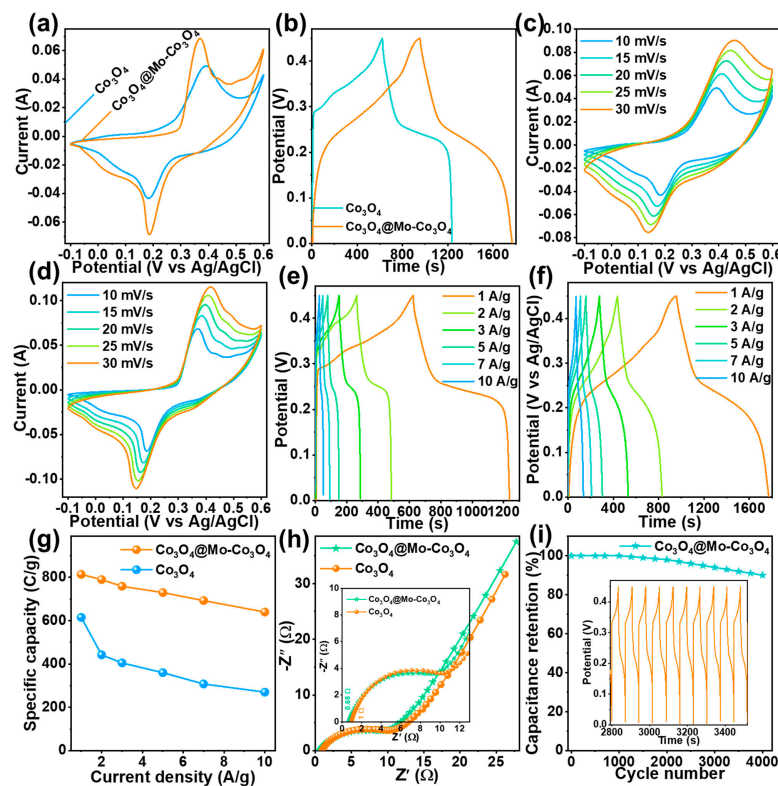


Figure 5. (a,b) Comparison plots of CV at 10 mV/s scan rate and GCD at 1 A/g current density for Co_3O_4 and the $\text{Co}_3\text{O}_4@\text{Mo-Co}_3\text{O}_4$ heterostructure, (c,d) CV curves at scan rates of 10 – 30 mV/s, (e,f) GCD curves at current densities of 1 – 10 A/g, (g) calculated specific capacity values from GCD curves, (h) Nyquist plot of Co_3O_4 and the $\text{Co}_3\text{O}_4@\text{Mo-Co}_3\text{O}_4$ heterostructure, (i) capacitance retention over 4000 GCD cycles; inset: ten consecutive GCD cycles.

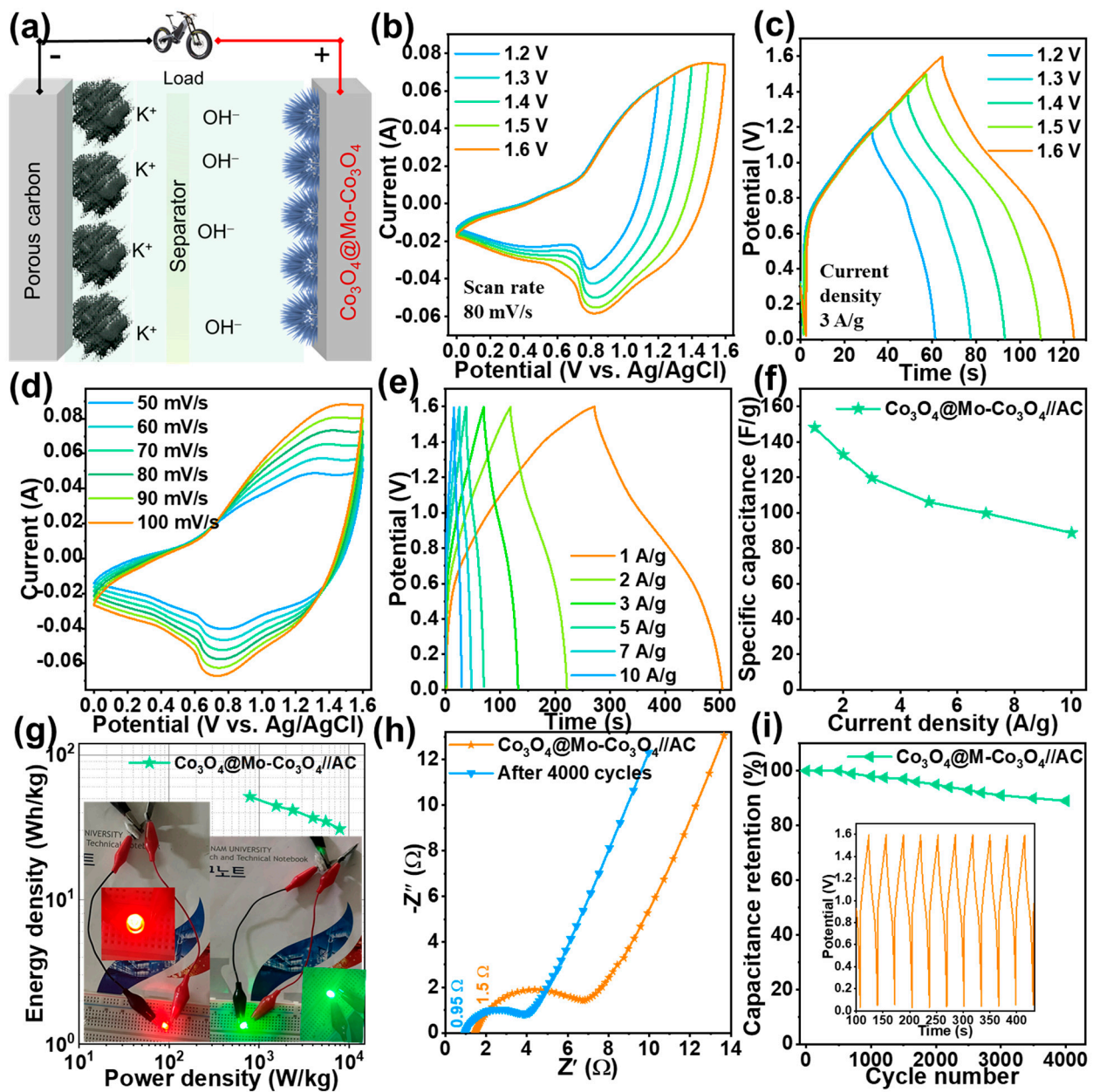


Figure 6. (a) Schematic of ASC device, (b) CV curves for different voltage windows at an 80-mV/s scan rate, (c) GCD curves for different voltage windows at a current density of 3 A/g (d,e) CV curves at scan rates of 50–100 mV/s and GCD curves at current densities of 1–10 A/g, (f) calculated specific capacitance values, (g) Power density vs. energy density plot, (h) Nyquist plot of before and after 4000 GCD cycles, (i) capacitance retention over 4000 GCD cycles; inset: ten consecutive GCD cycles of $\text{Co}_3\text{O}_4@Mo\text{-Co}_3\text{O}_4//AC$ ASC device.

The advantage of Mo-doping is to facilitate the electrochemical ability. The heterostructure formed by the addition of Mo improved the charge storage capacity by 30%. The pristine Co_3O_4 electrode exhibited a specific capacity of 615 C/g (1464 F/g), whereas the $\text{Co}_3\text{O}_4@Mo\text{-Co}_3\text{O}_4$ needle-like nanosheet heterostructure had a specific capacity of 814 C/g (1850 F/g). Besides Mo-doping, the enhanced electrochemical performance could be attributed to the heterostructure architecture of the obtained nanomaterials. The $Mo\text{-Co}_3\text{O}_4$ flower-like nanosheets provided a large area, leading to better electrolyte diffusion into the electrodes. In addition, the $Mo\text{-Co}_3\text{O}_4$ flower-like nanosheets provided an active electrochemical surface for redox reactions. The self-supported structure comprised a large

surface area for charge storage and fast electron transfer reactions. The advantages of this morphology are reflected in the Nyquist plot given in Figure 5h. The solution resistance was found to be 1 Ω and 0.65 Ω for Co_3O_4 and for the $\text{Co}_3\text{O}_4@\text{Mo-Co}_3\text{O}_4$ heterostructure, respectively (inset in Figure 5h). However, the reduced resistance would have increased the charge kinetics during the electrochemical process. Further, the stability test for 4000 cycles of continuous charge/discharge process in the KOH electrolyte was done with the $\text{Co}_3\text{O}_4@\text{Mo-Co}_3\text{O}_4$ heterostructure electrode. Even at the 4000th cycle, around 90% capacity retention was observed for the $\text{Co}_3\text{O}_4@\text{Mo-Co}_3\text{O}_4$ electrode. The inset of the last 10 similar GCD cycles corroborates the structural stability of the $\text{Co}_3\text{O}_4@\text{Mo-Co}_3\text{O}_4$ heterostructure electrode during long-term cycling. Thus, the excellent morphology and crystallinity of the $\text{Co}_3\text{O}_4@\text{Mo-Co}_3\text{O}_4$ needle-like nanosheet heterostructure electrode indicate that it is a very promising electrode material for supercapacitor applications.

3.2. Electrochemical Properties of a $\text{Co}_3\text{O}_4@\text{Mo-Co}_3\text{O}_4//\text{AC}$ Device

For practical applications, the $\text{Co}_3\text{O}_4@\text{Mo-Co}_3\text{O}_4$ heterostructure electrode was assembled with an AC electrode in a KOH electrolyte as an asymmetric supercapacitor, as represented in Figure 6a. The comparative CV curves of the negative AC and positive $\text{Co}_3\text{O}_4@\text{Mo-Co}_3\text{O}_4$ electrodes are presented in Figure S1. The asymmetric ($\text{Co}_3\text{O}_4@\text{Mo-Co}_3\text{O}_4//\text{AC}$) device potential window was optimized, as shown in Figure 6b,c. The CV curves in Figure 6b at 80 mV/s and the GCD profile at a current density of 3 A/g (Figure 6c) were made at different potential windows. The optimum potential window for the constructed device was found to be 0–1.6 V. The CV curves for the device were obtained at different scan rates, i.e., 50–100 mV/s, and GCD curves at various current densities, i.e., 1–10 A/g, as demonstrated in Figure 6d,e.

The calculated specific capacity for the $\text{Co}_3\text{O}_4@\text{Mo-Co}_3\text{O}_4//\text{AC}$ device is shown in Figure 6f. It showed a maximum capacitance of 154.6 F g^{-1} at a current density of 1 A g^{-1} . The superior supercapacitor performance might be accredited to the strong self-supported structure. The Ragone plot (Figure 6g) illustrated the energy and power density of the asymmetric $\text{Co}_3\text{O}_4@\text{Mo-Co}_3\text{O}_4//\text{AC}$ device. The device exhibited an energy density of 51.35 Wh/kg at a power density of 790 W/kg. The values of $\text{Co}_3\text{O}_4@\text{Mo-Co}_3\text{O}_4//\text{AC}$ device from the GCD are shown in Table 3, affirms improved capacitive performance of fabricated $\text{Co}_3\text{O}_4@\text{Mo-Co}_3\text{O}_4//\text{AC}$ device compared to previously reported works.

Table 3. Various electrochemical properties of Co_3O_4 -related materials compared to previous reports.

Electrode	Electrolyte	Specific Capacitance	Retention Rate	Energy Density (Wh kg^{-1})	Power Density (W kg^{-1})	Ref.
$\text{Mn@Co}_3\text{O}_4$	2M KOH	773 F g^{-1}	73.9%/5000 cycles	NA	NA	[29]
$\text{Mn-Co}_3\text{O}_4/\text{NF}$	2M KOH	668.4 F g^{-1}	104%/10,000	10.63	14,700	[30]
$\text{V-Co}_3\text{O}_4$	3M KOH	1593 F g^{-1}	NA	66.88	240	[31]
$\text{Fe-Co}_3\text{O}_4$	6M KOH	767.9 C g^{-1}	90%/4000	37	750	[32]
$\text{Cr, Sn-Co}_3\text{O}_4$	3M KOH	1413.56 F g^{-1}	89.41%/3000	NA	NA	[33]
$\text{Ce-Co}_3\text{O}_4$	3M KOH	1309.6 F g^{-1}	90.86%/2000	NA	NA	[34]
$\text{Mo-Co}_3\text{O}_4$	2M KOH	1850 F g^{-1}	90%/4000	–	–	This
$\text{Mo-Co}_3\text{O}_4//\text{AC}$	2M KOH	148 F g^{-1}	89%/4000	51.4	790	Work

The EIS study summarized in Figure 6h reveals minimal increase in solution resistance, even after 4000 cycles of charge/discharge. As shown in Figure 6i, the high retention (89%) also proved the long-term durability of the asymmetric device. Thus, the $\text{Co}_3\text{O}_4@\text{Mo-Co}_3\text{O}_4//\text{AC}$ device is promising for use in advanced electronics. Such significant electrochemical outcomes could be attributed to the crystallinity and morphology of the $\text{Co}_3\text{O}_4@\text{Mo-Co}_3\text{O}_4$ needle-like nanosheet heterostructure electrode, the self-supported structure with good mechanical and chemical stability, and the numerous nanoneedles, which offer enough surface area and active sites for electrochemical reactions and elec-

trolyte intake. Additionally, the one-pot synthesis of the aforementioned heterostructure is a facile, rapid and cheap method.

4. Conclusions

A novel $\text{Co}_3\text{O}_4@\text{Mo-Co}_3\text{O}_4$ nanosheet composite for supercapacitor applications was synthesized and its physical/electrochemical characteristics were investigated. The $\text{Co}_3\text{O}_4@\text{Mo-Co}_3\text{O}_4$ nanosheet composite achieved a superior specific capacity of 814 C g^{-1} at 1 A g^{-1} and capacity retention of 90% with a good rate capability. The asymmetric SC fabricated using this composite material achieved a capacitance of 154.6 F g^{-1} at 1 A g^{-1} , a specific energy of 51.35 Wh Kg^{-1} , and a specific power of 790 W kg^{-1} . Moreover, the $\text{Co}_3\text{O}_4@\text{Mo-Co}_3\text{O}_4//\text{AC}$ device possesses superior rate capabilities and long cycles, with 89.7% of the starting capacitance remaining after 4000 continuous cycles at 2 A g^{-1} . From this work, it may be concluded that the nanocomposite $\text{Co}_3\text{O}_4@\text{Mo-Co}_3\text{O}_4$ nanosheets coated over a Ni foam skeleton displayed superior capacities and could be considered for use in ultra-capacitor devices in the future.

Supplementary Materials: The following supporting information can be downloaded at: <https://www.mdpi.com/article/10.3390/nano12142330/s1>. Figure S1. The Rietveld refinement pattern of $\text{Co}_3\text{O}_4@\text{Mo-Co}_3\text{O}_4$ heterostructure; Figure S2. FTIR spectra of Co_3O_4 and $\text{Co}_3\text{O}_4@\text{Mo-Co}_3\text{O}_4$ composite; Figure S3. CV curves of two electrodes positive and negative.

Author Contributions: Conceptualization, I.M.O., Y.A.K., M.R.P. and S.A.; Supervision and validation, I.M.O. and S.A.; Investigation and writing, Y.A.K., M.R.P. and I.M.O.; Investigation and visualization, P.R.G. and H.T.D.; Validation, R.R.N.; All authors have read and agreed to the published version of the manuscript.

Funding: This work was financially supported by the UAEU-Strategic research program under Grant no. 12R128.

Data Availability Statement: No new data were created or analyzed in this study. Data sharing is not applicable to this article.

Acknowledgments: This work was financially supported by the UAEU-Strategic research program under Grant no. 12R128.

Conflicts of Interest: The authors declare no conflict of interest.

References

1. Yoon, J.H.; Kumar, Y.A.; Sambasivam, S.; Hira, S.A.; Krishna, T.N.V.; Zeb, K.; Uddin, W.; Kumar, K.D.; Obaidat, I.M.; Kim, S.; et al. Highly efficient copper-cobalt sulfide nano-reeds array with simplistic fabrication strategy for battery-type supercapacitors. *J. Energy Storage* **2020**, *32*, 101988. [[CrossRef](#)]
2. Mun, C.H.; Gopi, C.V.V.M.; Vinodh, R.; Sambasivam, S.; Obaidat, I.M.; Kim, H.J. Microflower-like nickel sulfide-lead sulfide hierarchical composites as binder-free electrodes for high-performance supercapacitors. *J. Energy Storage* **2019**, *26*, 100925. [[CrossRef](#)]
3. Das, H.T.; Mahendraprabhu, K.; Maiyalagan, T.; Elumalai, P. Performance of Solid-state Hybrid Energy-storage Device using Reduced Graphene-oxide Anchored Sol-gel Derived Ni/NiO Nanocomposite. *Sci. Rep.* **2017**, *7*, 15342. [[CrossRef](#)] [[PubMed](#)]
4. Duraisamy, E.; Das, H.T.; Sharma, A.S.; Elumalai, P. Supercapacitor and photocatalytic performances of hydrothermally-derived $\text{Co}_3\text{O}_4/\text{CoO}@$ carbon nanocomposite. *New J. Chem.* **2018**, *42*, 6114–6124. [[CrossRef](#)]
5. Yedluri, A.K.; Kim, H.-J. Wearable super-high specific performance supercapacitors using a honeycomb with folded silk-like composite of NiCo_2O_4 nanoplates decorated with NiMoO_4 honeycombs on nickel foam. *Dalton Trans.* **2018**, *47*, 15545–15554. [[CrossRef](#)]
6. Yedluri, A.K.; Anitha, T.; Kim, H.-J. Fabrication of Hierarchical $\text{NiMoO}_4/\text{NiMoO}_4$ Nanoflowers on Highly Conductive Flexible Nickel Foam Substrate as a Capacitive Electrode Material for Supercapacitors with Enhanced Electrochemical Performance. *Energies* **2019**, *12*, 1143. [[CrossRef](#)]
7. Hussain, S.; Khan, A.J.; Arshad, M.; Javed, M.S.; Ahmad, A.; Ahmad Shah, S.S.; Khan, M.R.; Akram, S.; Zulfiqar; Ali, S.; et al. Charge storage in binder-free 2D-hexagonal CoMoO_4 nanosheets as a redox active material for pseudocapacitors. *Ceram. Int.* **2021**, *47*, 8659–8667. [[CrossRef](#)]
8. Li, P.; Ruan, C.; Xu, J.; Xie, Y. Supercapacitive performance of CoMoO_4 with oxygen vacancy porous nanosheet. *Electrochim. Acta* **2020**, *330*, 135334. [[CrossRef](#)]

9. Theerthagiri, J.; Durai, G.; Tatarchuk, T.; Sumathi, M.; Kuppusami, P.; Qin, J.; Choi, M.Y. Synthesis of hierarchical structured rare earth metal-doped Co_3O_4 by polymer combustion method for high performance electrochemical supercapacitor electrode materials. *Ionics* **2020**, *26*, 2051–2061. [[CrossRef](#)]
10. Gopi, C.V.V.M.; Vinodh, R.; Sambasivam, S.; Obaidat, I.M.; Kalla, R.M.N.; Kim, H.J. One-pot synthesis of copper oxide-cobalt oxide core-shell nanocactus-like heterostructures as binder-free electrode materials for high-rate hybrid supercapacitors. *Mater. Today Energy* **2019**, *14*, 100358. [[CrossRef](#)]
11. Kumar, Y.A.; Sambasivam, S.; Hira, S.A.; Zeb, K.; Uddin, W.; Krishna, T.N.V.; Kumar, K.D.; Obaidat, I.M.; Kim, H.J. Boosting the energy density of highly efficient flexible hybrid supercapacitors via selective integration of hierarchical nanostructured energy materials. *Electrochim. Acta* **2020**, *364*, 137318. [[CrossRef](#)]
12. Shen, H.; Yang, X.; Song, J.; Gao, H.; Wu, Z.; Yu, J.; Lei, W.; Yang, J.; He, G.; Hao, Q. Electrodeposited molybdenum-doped Co_3O_4 nanosheet arrays for high-performance and stable hybrid supercapacitors. *J. Solid State Electrochem.* **2022**, *26*, 353–363. [[CrossRef](#)]
13. Xia, X.; Lei, W.; Hao, Q.; Wang, W.; Wang, X. One-step synthesis of CoMoO_4 /graphene composites with enhanced electrochemical properties for supercapacitors. *Electrochim. Acta* **2013**, *99*, 253–261. [[CrossRef](#)]
14. Lin, L.; Li, L.; Hussain, S.; Zhao, S.; Wu, L.; Peng, X.; Hu, N. Hierarchical 3D NiCo_2O_4 @ ZnWO_4 core-shell structures as binder-free electrodes for all-solid-state supercapacitors. *Appl. Surf. Sci.* **2018**, *452*, 113–122. [[CrossRef](#)]
15. Pallavolu, M.R.; Banerjee, A.N.; Nallapureddy, R.R.; Joo, S.W. Urea-assisted hydrothermal synthesis of MnMoO_4 / MnCO_3 hybrid electrochemical electrode and fabrication of high-performance asymmetric supercapacitor. *J. Mater. Sci. Technol.* **2022**, *96*, 332–344. [[CrossRef](#)]
16. Zhao, J.; Li, Z.; Yuan, X.; Yang, Z.; Zhang, M.; Meng, A.; Li, Q. A High-Energy Density Asymmetric Supercapacitor Based on Fe_2O_3 Nanoneedle Arrays and NiCo_2O_4 / $\text{Ni}(\text{OH})_2$ Hybrid Nanosheet Arrays Grown on SiC Nanowire Networks as Free-Standing Advanced Electrodes. *Adv. Energy Mater.* **2018**, *8*, 1702787. [[CrossRef](#)]
17. Pallavolu, M.R.; Gaddam, N.; Banerjee, A.N.; Nallapureddy, R.R.; Kumar, Y.A.; Joo, S.W. Facile construction and controllable design of CoTiO_3 @ Co_3O_4 /NCNO hybrid heterojunction nanocomposite electrode for high-performance supercapacitors. *Electrochim. Acta* **2022**, *407*, 139868. [[CrossRef](#)]
18. Kumar, Y.A.; Kim, H.-J. Preparation and electrochemical performance of NiCo_2O_4 @ NiCo_2O_4 composite nanoplates for high performance supercapacitor applications. *New J. Chem.* **2018**, *42*, 19971–19978. [[CrossRef](#)]
19. Pallavolu, M.R.; Kumar, Y.A.; Mani, G.; Nallapureddy, R.R.; Parvathala, A.; Albaqami, M.D.; Karami, A.M.; Joo, S.W. A novel hybridized needle-like Co_3O_4 /N-CNO composite for superior energy storage asymmetric supercapacitors. *J. Alloys Compd.* **2022**, *908*, 164447. [[CrossRef](#)]
20. Pallavolu, M.R.; Anil Kumar, Y.; Nallapureddy, R.R.; Goli, H.R.; Narayan Banerjee, A.; Joo, S.W. In-situ design of porous vanadium nitride@carbon nanobelts: A promising material for high-performance asymmetric supercapacitors. *Appl. Surf. Sci.* **2022**, *575*, 151734. [[CrossRef](#)]
21. Pallavolu, M.R.; Nallapureddy, J.; Nallapureddy, R.R.; Neelima, G.; Yedluri, A.K.; Mandal, T.K.; Pejjai, B.; Joo, S.W. Self-assembled and highly faceted growth of Mo and V doped ZnO nanoflowers for high-performance supercapacitors. *J. Alloys Compd.* **2021**, *886*, 161234. [[CrossRef](#)]
22. Gong, Y.; Wang, Y.; Sun, G.; Jia, T.; Jia, L.; Zhang, F.; Lin, L.; Zhang, B.; Cao, J.; Zhang, Z. Carbon Nitride Decorated Ball-Flower like Co_3O_4 Hybrid Composite: Hydrothermal Synthesis and Ethanol Gas Sensing Application. *Nanomaterials* **2018**, *8*, 132. [[CrossRef](#)] [[PubMed](#)]
23. Farhadi, S.; Pourzare, K.; Sadeghinejad, S. Simple preparation of ferromagnetic Co_3O_4 nanoparticles by thermal dissociation of the $[\text{Co}(\text{NH}_3)_6](\text{NO}_3)_2$ complex at low temperature. *J. Nanostruct. Chem.* **2013**, *3*, 16. [[CrossRef](#)]
24. Liu, Y.; Zhu, G.; Ge, B.; Zhou, H.; Yuan, A.; Shen, X. Concave Co_3O_4 octahedral mesocrystal: Polymer-mediated synthesis and sensing properties. *CrystEngComm* **2012**, *14*, 6264–6270. [[CrossRef](#)]
25. Mariammal, R.N.; Ramachandran, K.; Kalaiselvan, G.; Arumugam, S.; Renganathan, B.; Sastikumar, D. Effect of magnetism on the ethanol sensitivity of undoped and Mn-doped CuO nanoflakes. *Appl. Surf. Sci.* **2013**, *270*, 545–552. [[CrossRef](#)]
26. Aghazadeh, M. Electrochemical preparation and properties of nanostructured Co_3O_4 as supercapacitor material. *J. Appl. Electrochem.* **2012**, *42*, 89–94. [[CrossRef](#)]
27. Khalil, T.E.; Soliman, S.M.; Khalil, N.A.; El-Faham, A.; Foro, S.; El-Dissouky, A. Synthesis, structure, X-ray photoelectron spectroscopy (XPS), and antimicrobial, anticancer, and antioxidant activities of Co (III) complexes based on the antihypertensive hydralazine. *Appl. Organomet. Chem.* **2022**, *36*, e6565. [[CrossRef](#)]
28. Li, Q.; Li, Y.; Zhao, J.; Zhao, S.; Zhou, J.; Chen, C.; Tao, K.; Liu, R.; Han, L. Ultrathin nanosheet-assembled hollow microplate CoMoO_4 array derived from metal-organic framework for supercapacitor with ultrahigh areal capacitance. *J. Power Sources* **2019**, *430*, 51–59. [[CrossRef](#)]
29. Chen, H.; Wang, J.; Liao, F.; Han, X.; Zhang, Y.; Xu, C.; Gao, L. Uniform and porous Mn-doped Co_3O_4 microspheres: Solvothermal synthesis and their superior supercapacitor performances. *Ceram. Int.* **2019**, *45*, 11876–11882. [[CrossRef](#)]
30. Li, G.; Chen, M.; Ouyang, Y.; Yao, D.; Lu, L.; Wang, L.; Xia, X.; Lei, W.; Chen, S.-M.; Mandler, D.; et al. Manganese doped Co_3O_4 mesoporous nanoneedle array for long cycle-stable supercapacitors. *Appl. Surf. Sci.* **2019**, *469*, 941–950. [[CrossRef](#)]
31. Niknam, E.; Naffakh-Moosavy, H.; Moosavifard, S.E.; Afshar, M.G. Multi-shelled bimetal V-doped Co_3O_4 hollow spheres derived from metal organic framework for high performance supercapacitors. *J. Energy Storage* **2021**, *44*, 103508. [[CrossRef](#)]

32. Cheng, L.; Zhang, Q.; Xu, M.; Zhai, Q.; Zhang, C. Two-for-one strategy: Three-dimensional porous Fe-doped Co_3O_4 cathode and N-doped carbon anode derived from a single bimetallic metal-organic framework for enhanced hybrid supercapacitor. *J. Colloid Interface Sci.* **2021**, *583*, 299–309. [[CrossRef](#)] [[PubMed](#)]
33. Ali, F.; Khalid, N.R.; Niaz, N.A.; Nabi, G.; Tahir, M.B.; Rafique, M. Novel Cr and Sn co-doped Co_3O_4 polygon-based electrode material for supercapacitor application. *J. Mater. Sci. Mater. Electron.* **2021**, *32*, 11467–11477. [[CrossRef](#)]
34. Ali, F.; Khalid, N.R.; Nabi, G.; Ul-Hamid, A.; Ikram, M. Hydrothermal synthesis of cerium-doped Co_3O_4 nanoflakes as electrode for supercapacitor application. *Int. J. Energy Res.* **2021**, *45*, 1999–2010. [[CrossRef](#)]